


Measuring ISW with next-generation radio surveys

Mario Ballardini^{1,2} , Roy Maartens^{1,3}

¹*Department of Physics & Astronomy, University of the Western Cape, Cape Town 7535, South Africa*

²*INAF/OAS Bologna, via Gobetti 101, I-40129 Bologna, Italy*

³*Institute of Cosmology & Gravitation, University of Portsmouth, Portsmouth PO1 3FX, UK*

17 March 2022

ABSTRACT

The late-time integrated Sachs-Wolfe (ISW) signal in the CMB temperature anisotropies is an important probe of dark energy when it can be detected by cross-correlation with large-scale structure surveys. Because of their huge volume, surveys in the radio are well-suited to ISW detection. We show that 21cm intensity mapping and radio continuum surveys with the SKA in Phase 1 promise a $\sim 5\sigma$ detection, with a similar forecast for the precursor EMU survey. In SKA2, the 21cm galaxy redshift survey could deliver a $\sim 6\sigma$ detection, which is probably the maximum achievable level. Our analysis includes the observational effects on the radio surveys of lensing magnification, Doppler and other relativistic corrections. These effects alter the shape of the measured ISW signal, especially at high redshift. The cross-correlation between lensing magnification and CMB temperature at high redshift is not a direct probe of dark energy and could bias the ISW reconstruction. We find that cross-correlation between different redshift bins compensates the shift due to adding the relativistic corrections in the ISW detection and improves the quality of the ISW reconstruction.

Key words: cosmology: observations – cosmic background radiation – large-scale structure of Universe.

1 INTRODUCTION

The late-time integrated Sachs-Wolfe (ISW) effect in the cosmic microwave background (CMB) arises from the time variation of the gravitational potentials along the line of sight (Sachs & Wolfe 1967). CMB photons are gravitational redshifted while travelling through potential wells and hills connected to matter over- and under-densities. In a matter-dominated universe the local gravitational potentials are constant and the net effect of a photon falling into a gravity well and coming out is zero. By contrast, gravitational potentials decay during the Λ -dominated phase, leading to a net change in photon temperature and in the observed CMB temperature anisotropies. These potential fluctuations are induced by density perturbations at relatively low redshifts and generate a non-vanishing cross-correlation component between CMB temperature anisotropies and CMB lensing, and between CMB temperature anisotropies and number count fluctuations.

Many measurements of the ISW signal based on cross-correlating the CMB with large-scale structure tracers have been performed (Crittenden & Turok 1996; Nolita et al. 2004; Fosalba & Gaztanaga 2004; Boughn & Crittenden 2004; Afshordi et al. 2004; Vielva et al. 2006; McEwen et al.

2007; Ho et al. 2008; Giannantonio et al. 2008; Hernandez-Montegudo 2010; Taburet et al. 2011; Ilic et al. 2011; Schiavon et al. 2012; Barreiro et al. 2013; Ade et al. 2014; Ferraro et al. 2015; Manzotti & Dodelson 2014; Ade et al. 2016; Shajib & Wright 2016; Bianchini et al. 2016; Stölzner et al. 2018). Measurements have used different matter tracers: radio source catalogues, spectroscopic and photometric galaxy surveys, photometric quasars, thermal Sunyaev-Zeldovich, cosmic infrared background, and CMB lensing. Alternatively, the stacking of CMB data in correspondence with superclusters and supervoids has also been used for ISW detection (Granett et al. 2008; Papai et al. 2011; Ilic et al. 2011; Ade et al. 2014, 2016).

ISW fluctuations contribute mainly to large angular scales, $\ell \lesssim 100$, of the CMB temperature angular power spectrum, since there is little power in the potentials at late times on scales that entered the Hubble radius during radiation domination (Kofman & Starobinsky 1985). For this reason, wide surveys are optimal to tackle ISW detection. Such surveys can probe the large-scale structure on ultra-large (super-equality) scales, facilitating measurements of not only the ISW, but also primordial non-Gaussianity, the primordial power spectrum and relativistic observational effects on number counts and intensity (Raccanelli et al. 2012; Maartens et al. 2013; Raccanelli et al. 2015; Camera et al. 2015; Raccanelli et al. 2016; Alonso et al. 2015; Fonseca et al.

* Contact e-mail: mario.ballardini@gmail.com

2015; Ballardini et al. 2018; Karagiannis et al. 2018; Bernal et al. 2018). Among the next-generation surveys of the large-scale structure, radio surveys promise to deliver the largest volumes, using neutral hydrogen (HI) 21cm emission or radio continuum emission of galaxies (Maartens et al. 2015). Radio surveys can maximise the synergies with CMB maps, thanks to their large overlapping sky area.

In order to perform a reliable reconstruction and detection of the ISW signal we must understand the impact of different systematics, for instance effects due to incomplete sky coverage (Bonavera et al. 2016), calibration errors (Afshordi 2004; Muir & Huterer 2016; Weaverdyck et al. 2018), and uncertainties on the source redshift distribution and bias model (Afshordi 2004; Hernandez-Monteagudo 2010; Ballardini et al. 2019). In addition, systematics need to be taken into account in the reconstruction estimator to avoid biased results (Muir & Huterer 2016; Weaverdyck et al. 2018).

In this paper, we test the feasibility of detecting the ISW signal with future cosmological surveys in Phase 1 of the Square Kilometre Array (SKA) (Bacon et al. 2018), together with two of its precursor surveys, MeerKLASS (Santos et al. 2017) and EMU (Norris et al. 2011). We also consider the more futuristic ‘billion galaxy’ SKA2 spectroscopic survey.

We begin by quantifying the theoretical signal-to-noise ratio (SNR) for ISW detection through angular cross-power spectra of CMB temperature and number count/ intensity. Then we simulate ISW and large-scale structure (LSS) maps to identify the quality of the reconstruction for the radio surveys considered. We explore the impact of the lensing magnification and other relativistic effects in LSS maps on the cross-correlation with CMB temperature maps (see also Challinor & Lewis 2011; LoVerde et al. 2007; Renk et al. 2016). When these effects are not modelled, there is a degradation of the ISW reconstruction. In addition, we highlight the importance of the cross-correlations between redshift bins when a tomographic approach to these surveys is used.

The paper is organized as follows. We review the angular cross-power spectrum in section 2, and the SNR calculation in section 3. In section 4, we describe the properties of the surveys. Section 5 discusses our results for the SNR analysis. Our procedure for ISW reconstruction is described in section 6, together with discussion on the accuracy of using the average correlation coefficient and on map residuals between the true ISW map and the reconstructed one in pixel space. We draw our conclusions in section 7.

2 CMB-LSS CROSS-CORRELATION

We study the cross-correlation between the LSS angular power spectrum derived in linear perturbation theory assuming general relativity (GR) and the ISW contribution to the CMB temperature angular power spectrum. There is a simple way to relate number count results to intensity mapping, which we describe below. Therefore in this section we consider the observed number counts for a magnitude-limited survey.

In Newtonian gauge and in Fourier space, the multipoles of the observed number counts can be split into a standard term, which includes redshift space distortions (RSD) by convention, and the GR contributions which are effectively

the corrections to the standard Newtonian approximation:

$$\Delta_\ell(\mathbf{k}, z) = \Delta_\ell^N(\mathbf{k}, z) + \Delta_\ell^{\text{GR}}(\mathbf{k}, z). \quad (1)$$

The standard term is the number density contrast plus the standard RSD term:

$$\Delta_\ell^N = b \delta_{\mathbf{k}}^c j_\ell(k\chi) + \frac{k v_{\mathbf{k}}}{\mathcal{H}} j_\ell'(k\chi). \quad (2)$$

Here $\delta_{\mathbf{k}}^c(z)$ is the comoving matter density contrast, used in order to impose a physical model of scale-independent bias $b(z)$ (Challinor & Lewis 2011; Bruni et al. 2012; Jeong et al. 2012; Baldauf et al. 2012). The peculiar velocity of the source is \mathbf{v} , with $v_{\mathbf{k}}(z) = |\mathbf{v}_{\mathbf{k}}(z)|$, and j_ℓ are spherical Bessel functions, where prime denotes $d/d(k\chi)$. $\mathcal{H}(z) = (1+z)^{-1}H(z)$ is the conformal Hubble parameter and $\chi(z)$ is the comoving distance.

The GR corrections (Challinor & Lewis 2011) are given by the lensing convergence contribution, the Doppler effect due to redshift perturbations from peculiar velocity, and ultra-large scale terms (ULS) from the gravitational potentials, which are $\propto (\mathcal{H}/k)^2 \delta_{\mathbf{k}}^c$. The gravitational potentials are defined by:

$$ds^2 = [-(1+2\psi)d\eta^2 + (1-2\phi)d\mathbf{x}^2]. \quad (3)$$

In detail (Fonseca et al. 2015):

$$\Delta_\ell^{\text{GR}} \equiv \Delta_\ell^{\text{L}} + \Delta_\ell^{\text{V}} + \Delta_\ell^{\text{ULS}}, \quad (4)$$

$$\Delta_\ell^{\text{L}} = \frac{\ell(\ell+1)}{2} (2-5s) \times \int_0^x d\tilde{\chi} \frac{(\chi-\tilde{\chi})}{\chi\tilde{\chi}} [\psi_{\mathbf{k}}(\tilde{\chi}) + \phi_{\mathbf{k}}(\tilde{\chi})] j_\ell(k\tilde{\chi}), \quad (5)$$

$$\Delta_\ell^{\text{V}} = \left[\frac{2-5s}{\mathcal{H}\chi} + 5s - b_e + \frac{\dot{\mathcal{H}}}{\mathcal{H}^2} \right] v_{\mathbf{k}} j_\ell'(k\chi), \quad (6)$$

where

$$s(z, m_*) = \frac{\partial \log \bar{N}(z, m < m_*)}{\partial m_*}, \quad (7)$$

$$b_e(z, m_*) = -\frac{\partial \ln[(1+z)^{-3} \bar{N}(z, m < m_*)]}{\partial \ln(1+z)} \quad (8)$$

are the magnification bias and evolution bias, and \bar{N} is the background number density of sources with luminosity above the threshold.

The ULS contribution is made up of local and integrated terms – the latter are a number-count ISW term and a time-delay term:

$$\Delta_\ell^{\text{ULS}} = \left\{ \left[\frac{2-5s}{\mathcal{H}\chi} + 5s - b_e + \frac{\dot{\mathcal{H}}}{\mathcal{H}^2} + 1 \right] \psi_{\mathbf{k}} + (5s-2)\phi_{\mathbf{k}} + \frac{\dot{\phi}_{\mathbf{k}}}{\mathcal{H}} + (b_e-3)\mathcal{H} \frac{v_{\mathbf{k}}}{k} \right\} j_\ell(k\chi) + \left[\frac{2-5s}{\mathcal{H}\chi} + 5s - b_e + \frac{\dot{\mathcal{H}}}{\mathcal{H}^2} \right] \int_0^x d\tilde{\chi} [\dot{\psi}_{\mathbf{k}}(\tilde{\chi}) + \dot{\phi}_{\mathbf{k}}(\tilde{\chi})] j_\ell(k\tilde{\chi}) + \frac{(2-5s)}{\chi} \int_0^x d\tilde{\chi} [\psi_{\mathbf{k}}(\tilde{\chi}) + \phi_{\mathbf{k}}(\tilde{\chi})] j_\ell(k\tilde{\chi}). \quad (9)$$

The velocity term $v_{\mathbf{k}}/k$ in (9) arises from expressing the Newtonian-gauge number density contrast in comoving gauge – it can be rewritten as a potential term using the Poisson and continuity equations.

The angular cross-power spectra of the observed number counts and of the CMB ISW are given by:

$$C_\ell^{XY} = 4\pi \int \frac{dk}{k} \mathcal{P}_{\mathcal{R}}(k) I_\ell^X(k) I_\ell^Y(k), \quad (10)$$

where $\mathcal{P}_{\mathcal{R}}(k)$ is the dimensionless primordial power spectrum and $X, Y = \Delta$ or ISW. The kernels are

$$I_{\ell}^{\Delta}(k) = \int dz W(z) \Delta_{\ell}(k, z), \quad (11)$$

$$I_{\ell}^{\text{ISW}}(k) = \int dz e^{-\tau(z)} \left[\dot{\phi}_{\mathbf{k}}(z) + \dot{\psi}_{\mathbf{k}}(z) \right] j_{\ell}(k\chi(z)), \quad (12)$$

where $W(z)$ is the normalized redshift distribution function, given by $W(z) \propto \bar{N}(z)$ (and $W(z) \propto \bar{T}_{\text{HI}}(z)$ for intensity mapping), and τ is the optical depth.

In order to split the LSS survey into redshift bins $z_i \pm \Delta z/2$, we include a top-hat window function for HI surveys (which have excellent spectroscopic accuracy), and a Gaussian distribution for the continuum survey, $W(z_i) \propto \bar{N}(z_i)w(z_i)$.

The most relevant source of noise in a clustering analysis of discrete sources is shot noise, determined by the number density, $\mathcal{N}_{\ell}(z_i) = 1/\bar{n}_i$ where:

$$\bar{n}_i = \int dz \bar{N}(z_i)w(z_i), \quad (13)$$

is the integral of the redshift distribution over the i -bin.

3 THEORETICAL SIGNAL-TO-NOISE

In order to quantify the possibility to extract the ISW signal from the CMB we use the signal-to-noise ratio (SNR), following (Cooray 2002; Afshordi 2004):

$$\left(\frac{S}{N} \right)^2 = \sum_{\ell=2}^{\ell_{\text{max}}} \left(\mathbf{C}_{\ell}^{\Delta \text{ ISW}} \right)^{\dagger} \left(\mathbf{C}_{\ell}^{\text{cov}} \right)^{-1} \mathbf{C}_{\ell}^{\Delta \text{ ISW}}. \quad (14)$$

Here $\mathbf{C}_{\ell}^{\Delta \text{ ISW}}$ is the vector of the angular cross-power spectra, and the covariance matrix elements are:

$$\mathbf{C}_{\ell}^{\text{cov}}(z_i, z_j) = \frac{C_{\ell}^{\Delta \text{ ISW}}(z_i) C_{\ell}^{\Delta \text{ ISW}}(z_j) + \bar{C}_{\ell}^{\Delta}(z_i, z_j) \bar{C}_{\ell}^{\text{ISW}}}{(2\ell + 1) f_{\text{sky}}}. \quad (15)$$

Here f_{sky} is the common sky fraction covered by the two surveys and an overbar denotes the sum of the signal and its noise. For the ISW contribution to the CMB, the primary temperature auto-power is part of the noise:

$$\bar{C}_{\ell}^{\text{ISW}} = C_{\ell}^{\text{ISW}} + C_{\ell}^{\text{TT}} + \mathcal{N}_{\ell}^{\text{T}}. \quad (16)$$

At low and intermediate multipoles, where the ISW signal is not suppressed, the instrumental noise on the CMB temperature signal can be neglected, i.e. $\mathcal{N}_{\ell}^{\text{T}} \approx 0$.

The CMB E-mode polarization can be used to track better the ISW signal in the CMB temperature angular power spectrum, thanks to the TE correlation between the two spectra. By including the E-mode polarization information, it is possible to decrease the effective cosmic variance on the CMB temperature and ISW angular power spectra:

$$\bar{C}_{\ell}^{\text{ISW}} = C_{\ell}^{\text{ISW}} + C_{\ell}^{\text{TT}} - \frac{(C_{\ell}^{\text{TE}})^2}{C_{\ell}^{\text{EE}}} + \mathcal{N}_{\ell}^{\text{T}}. \quad (17)$$

The inclusion of CMB polarization in the analysis increases the SNR by $\sim 18\%$ (Frommert & Ensslin 2008; Giannantonio et al. 2012; Ballardini et al. 2019). Therefore in the SNR calculation we always include the E-mode polarization information according to (17).

4 RADIO SURVEY SPECIFICATIONS

In this section we provide the LSS survey details used for the analysis. For the CMB we use *Planck* (Ade et al. 2016) simulated data.

4.1 HI intensity mapping survey

HI intensity mapping (IM) surveys do not attempt to detect individual HI galaxies, but measure the total signal in each pixel to produce maps of the large-scale fluctuations in HI galaxy clustering (with very accurate redshifts) (Battye et al. 2004; Wyithe & Loeb 2008; Chang et al. 2008; Bull et al. 2015; Santos et al. 2015; Kovetz et al. 2017). The flux density measured is converted into an effective brightness temperature of the 21cm emission:

$$T_{\text{HI}} = \bar{T}_{\text{HI}}(1 + \delta_{\text{HI}}) \mu\text{K}. \quad (18)$$

HI is expected to be a biased tracer of the cold dark matter distribution, just as galaxies are, because the HI content of the Universe is expected to be localized within galaxies after reionization. We use the fitting formulas (Santos et al. 2017):

$$b_{\text{HI}}(z) = \frac{b_{\text{HI}}(0)}{0.677105} \left[0.66655 + 0.17765 z + 0.050223 z^2 \right], \quad (19)$$

$$\bar{T}_{\text{HI}}(z) = 0.055919 + 0.23242 z - 0.024136 z^2 \mu\text{K}, \quad (20)$$

where $\Omega_{\text{HI}}(0)b_{\text{HI}}(0) = 4.3 \times 10^{-4}$ and $\Omega_{\text{HI}}(0) = 4.86 \times 10^{-4}$.

The observed brightness temperature contrast may be obtained from the number count case by using effective values for the evolution and magnification biases as follows (Hall et al. 2013; Fonseca et al. 2018):

$$b_{\text{eHI}}(z) = -\frac{\partial \ln [(1+z)^{-1} \mathcal{H}(z) \bar{T}_{\text{HI}}(z)]}{\partial \ln(1+z)}, \quad s_{\text{HI}} = \frac{2}{5}. \quad (21)$$

Note that the lensing magnification contribution is thus zero at first order.

We consider IM in single-dish mode, using SKA1-MID Band 1 and the proposed IM survey MeerKLASS on the precursor MeerKAT. Single-dish mode is the most efficient way to probe cosmological scales with IM (Santos et al. 2015). Assuming scale-independence and no correlation between the noise in different frequency channels, the noise variance per steradian in the i -frequency channel is (Knox 1995; Bull et al. 2015):

$$\mathcal{N}_{\ell}^{\text{HI}}(\nu_i) = \frac{4\pi f_{\text{sky}} T_{\text{sys}}^2(\nu_i)}{2N_{\text{dish}} t_{\text{tot}} \Delta\nu}, \quad (22)$$

$$T_{\text{sys}}(\nu) = 25 + 60 \left(\frac{300 \text{ MHz}}{\nu} \right)^{2.55} \text{ K}. \quad (23)$$

For MeerKLASS, we assume $N_{\text{dish}} = 64$, $t_{\text{tot}} = 4,000$ hr over $4,000 \text{ deg}^2$ ($f_{\text{sky}} \simeq 0.1$) in the redshift ranges $0 \leq z \leq 0.58$ ($1670 \geq \nu \geq 900 \text{ MHz}$, L Band) and $0.4 \leq z \leq 1.45$ ($1015 \geq \nu \geq 580 \text{ MHz}$, UHF Band) (Santos et al. 2017).

For SKA1-MID, we assume $N_{\text{dish}} = 197$, $t_{\text{tot}} = 10^4$ hr observing over $20,000 \text{ deg}^2$ ($f_{\text{sky}} \simeq 0.5$) in the redshift range $0.35 \leq z \leq 3.05$ ($1050 \geq \nu \geq 350 \text{ MHz}$, Band 1) (Bacon et al. 2018).

4.2 Radio continuum survey

For a continuum galaxy survey with SKA1-MID, we assume the same frequency band and sky area as for the IM survey, with a source detection limit $S_{\text{cut}} = 22 \mu\text{Jy}$ (Bacon et al. 2018). We study also an optimistic case for SKA1-MID with $S_{\text{cut}} = 10 \mu\text{Jy}$. For SKA2 we assume $f_{\text{sky}} \simeq 0.7$ and $S_{\text{cut}} = 1 \mu\text{Jy}$.

As an SKA precursor continuum galaxy survey, we consider EMU on ASKAP (Norris et al. 2011; Bernal et al. 2018), a $30,000 \text{ deg}^2$ ($f_{\text{sky}} \simeq 0.7$) survey over the frequency range 700-1450 MHz with source detection limit $100 \mu\text{Jy}$.

The redshift distribution, bias, magnification bias and evolution bias are predicted using the publicly available code¹ developed by Alonso et al. (2015), which provides semi-analytical fits based on the simulations described in Wilman et al. (2008).

4.3 HI galaxy survey

The models for the number counts and the clustering, evolution and magnification biases of the HI galaxy distribution are given in Camera et al. (2015), for various flux thresholds.

For SKA1, the sky area and redshift coverage are too low for detecting the ISW. SKA2 specifications have not been formalised, but the rms noise is expected to be ~ 10 times smaller than SKA1, and the sky coverage increased from $20,000$ to $30,000 \text{ deg}^2$ ($f_{\text{sky}} \simeq 0.7$). We assume a total observation time of 10^4 hr in a redshift range $0.1 \leq z \leq 2$, and with flux threshold $1 \mu\text{Jy}$. This is the so-called ‘billion galaxy’ survey.

5 RESULTS

5.1 HI IM survey

Table 1 summarises the SNR obtained by cross-correlating the observed HI brightness temperature contrast Δ_{HI} with the ISW signal. We calculate the SNR for two different configurations, for MeerKAT L-band/ UHF-band/ SKA1-MID Band 1 respectively:

$$1 \text{ } z\text{-bin with edges } [0, 0.58]/[0.4, 1.45]/[0.35, 3.05] \quad (24)$$

$$5/11/27 \text{ } z\text{-bins with } \Delta z = 0.1 \quad (25)$$

The SNR for MeerKAT IM surveys is strongly limited by the survey area of $4,000 \text{ deg}^2$. Moreover, the instrumental noise limits the possibility to increase the SNR by considering many slices in redshift. We find a $\text{SNR} \sim 1.1 - 1.3$ for the L-band and $\sim 1.7 - 1.9$ for the UHF-band. For an SKA1-MID Band 1 IM survey, we find a SNR of ~ 3.7 using the whole survey as one single redshift bin, up to ~ 4.7 using tomography.

In IM the lensing magnification contribution given by (5) is zero by (21). As a further consequence of $s_{\text{HI}} = 2/5$, many other terms in (4) related to Doppler and gravitational potentials vanish. We find that the contribution from the remaining GR corrections in the observed temperature contrast Δ_{HI} is much smaller than the Newtonian $\Delta_{\text{HI}}^{\text{N}}$ contribution, even at high redshift. This can be seen in figure 1.

Therefore there is a negligible shift in the SNR compared to the Newtonian approximation, as is evident in table 1.

We note that including the cross-correlations between redshift bins in (14) increases the SNR, especially for SKA1.

In Pourtsidou et al. (2017), the SNR for the ISW detection is calculated for MeerKAT UHF-band and SKA1-MID Band 1 assuming independent redshift bins with a width of $\Delta z = 0.1$. They find a SNR of 1.5 and 4.6, consistent with our findings. Small differences are due to their assumptions of: a different best-fit cosmology, a simplified redshift independent bias, i.e. $b_{\text{HI}}(z) = 1$, and a larger sky coverage of $30,000 \text{ deg}^2$.

5.2 Radio continuum survey

In table 2, we show the SNR obtained by cross-correlating the observed number counts Δ_g with the CMB ISW. This is done for EMU and SKA1 continuum surveys. We calculate the SNR for binning configurations:

$$1 \text{ } z\text{-bin with edges } [0, 5] \quad (26)$$

$$5 \text{ } z\text{-bins with edges } [0, 0.5, 1, 1.5, 2, 5] \quad (27)$$

The second configuration applies only to SKA1 and is given in Bacon et al. (2018), based on the argument that sufficient spectroscopic information will be found (from cross-matching with 21cm and optical/ infrared surveys) to construct $\Delta z = 0.5$ bins up to $z = 2$.

Thanks to the wide sky coverage, we find a SNR of ~ 5 for EMU, despite its higher flux threshold. We obtain a $\text{SNR} \sim 4.0 - 5.0$ for the SKA1 survey with the baseline $S_{\text{cut}} = 22 \mu\text{Jy}$. For the optimistic case of $S_{\text{cut}} = 10 \mu\text{Jy}$, we find $\text{SNR} \sim 5.1$ – it is interesting that the SNR in this case is not improved by having 5 redshift bins.

Continuum galaxy surveys are magnitude limited, so that $s(z) \neq 0$. Figure 2 shows that the lensing effect is very important at high redshift on the large scales where the ISW signal is stronger. The Δ^{L} -ISW contribution (dotted line) to the full cross-correlation angular power spectrum (solid line) is of the same order of magnitude as the Δ^{N} -ISW contribution (dashed line) for the highest redshift bins.

In figure 2, we also see that the cross-correlation between Δ^{L} and ISW is always negative (blue) and it is the dominant GR correction for $z \gtrsim 1$. This lensing contribution reduces the cross-power spectrum relative to the Newtonian approximation Δ^{N} -ISW. However, the difference is compensated at SNR level when cross-bin correlations are included, see table 2. Note also from table 2 that if we neglect cross-bin correlations, then we over-estimate the true SNR.

The SNR for SKA2, with a larger sky coverage of $30,000 \text{ deg}^2$ and a lower flux threshold of $1 \mu\text{Jy}$, is $\sim 5.6 - 6.2$.

5.3 HI galaxy survey

Table 3 summarises the SNR obtained for the number counts-ISW cross-correlation detection for an SKA2 HI galaxy survey. We use two binning configurations:

$$1 \text{ } z\text{-bin with edges } [0.1, 2] \quad (28)$$

$$19 \text{ } z\text{-bins with } \Delta z = 0.1 \quad (29)$$

We obtain a $\text{SNR} \sim 3.8 - 6.1$ considering the Newtonian term only for the number counts auto- and cross-spectra. Similar to the continuum galaxy survey, there is

¹ <http://intensitymapping.physics.ox.ac.uk/codes.html>

Table 1. SNR for ISW detection from IM surveys with MeerKAT and SKA1-MID, using binning configurations (24) and (25). SNR is calculated for the full HI temperature contrast Δ (left column) and its Newtonian approximation Δ^N (right column). Numbers in round brackets indicate neglect of the contribution from cross-correlations between z -bins in (14).

	MeerKLASS L-band		MeerKLASS UHF-band		SKA1-MID Band 1	
	Δ -ISW	Δ^N -ISW	Δ -ISW	Δ^N -ISW	Δ -ISW	Δ^N -ISW
1 bin	1.1	1.1	1.7	1.7	3.7	3.7
$\Delta z = 0.1$ bins	1.3 (1.2)	1.3 (1.2)	1.9 (1.6)	1.9 (1.6)	4.7 (3.9)	4.7 (3.9)

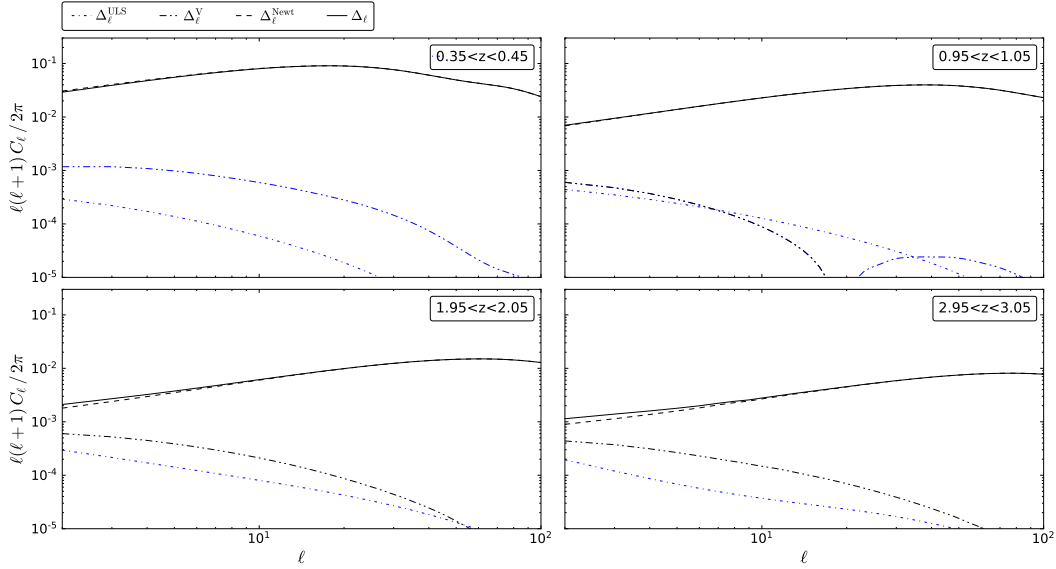


Figure 1. HI temperature contrast-ISW cross-correlation for an SKA1-MID IM survey, showing 4 of the 27 redshift bins. Different lines correspond to the contributions from ultra-large scale GR effects (Δ^{ULS} , dot-dashed), from Doppler effects (Δ^{V} , dot-dot-dashed), from the Newtonian approximation (Δ^N , dashed), and from the total (Δ , solid). Blue lines indicate the absolute value of a negative contribution.

Table 2. As in table 1 for ISW detection from continuum galaxy surveys with ASKAP and SKA1-MID, using binning configurations (26) and (27).

	EMU $S_{\text{cut}} = 100 \mu\text{Jy}$		SKA1-MID Band 1 $S_{\text{cut}} = 22 \mu\text{Jy}$		SKA1-MID Band 1 $S_{\text{cut}} = 10 \mu\text{Jy}$		SKA2 $S_{\text{cut}} = 1 \mu\text{Jy}$	
	Δ -ISW	Δ^N -ISW	Δ -ISW	Δ^N -ISW	Δ -ISW	Δ^N -ISW	Δ -ISW	Δ^N -ISW
1 bin	5.0	5.0	4.0	4.0	5.1	5.1	5.6	5.6
5 bins	—	—	5.0 (5.2)	5.0 (5.0)	5.1 (5.4)	5.1 (5.3)	6.2 (6.0)	6.2 (6.6)

a negative contribution to the total number counts-ISW cross-correlation due to lensing magnification Δ^L leading, to a $\text{SNR} \sim 3.7 - 6.0$. Figure 3 shows that in this case the Δ^L -ISW contribution to the observed number counts-ISW cross-correlation can be positive at smaller scales, leading to a higher SNR.

5.4 Cross-bin correlations

The calculation of the SNR (14) has been done with and without the cross-correlation between different redshift bins:

the results neglecting the cross-bin correlations are in brackets in tables 1–3. We find that the inclusion of cross-bin correlations has an important impact on the SNR. In particular, it compensates the shift induced by adding the GR effects in the ISW detection. In fact, the lensing contribution (which dominates the GR effects) induces a correlation between high and low redshift, where the high redshifts are only probing the low redshift large scales. The correlation between high and low redshift is due to the lensing of high redshift sources from all the sources nearest to us. This gives the possibility to extract information from low redshift physics us-

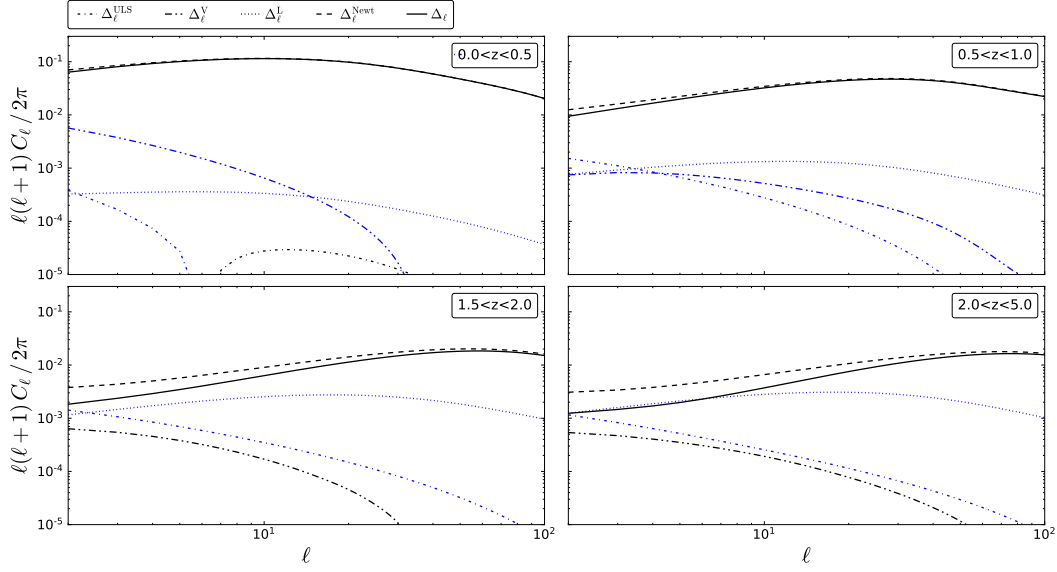


Figure 2. As in figure 1, for an SKA1 continuum survey ($S_{\text{cut}} = 22 \mu\text{Jy}$), showing 4 of the 5 redshift bins. The lensing contribution, absent in figure 1, is Δ^L (dotted).

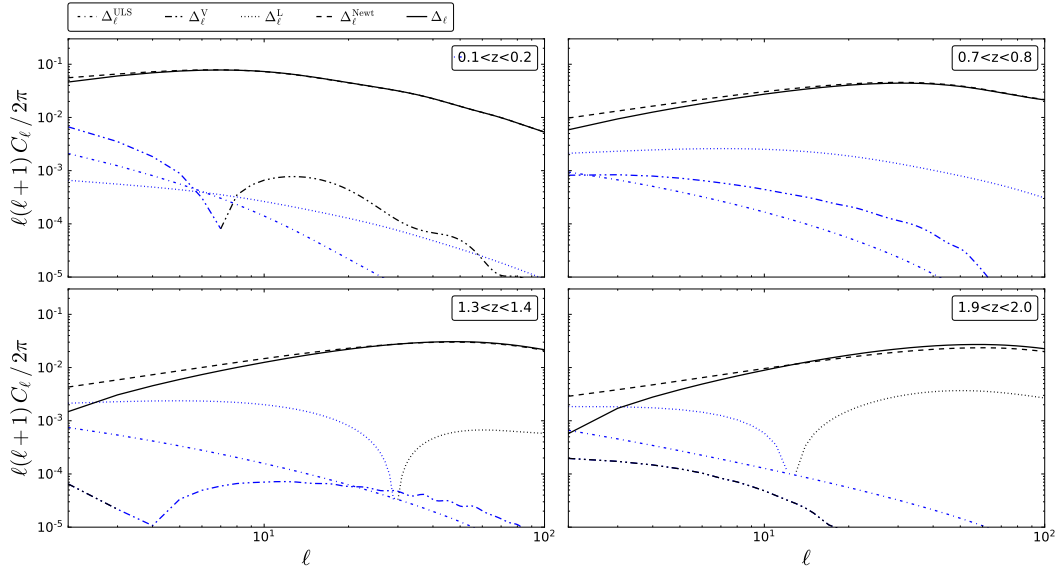


Figure 3. As in figures 1–2, for an SKA2 HI galaxy survey, showing 4 of the 19 redshift bins.

Table 3. As in tables 1–2, for an SKA2 HI galaxy survey, using binning configurations (28) and (29).

	SKA2	
	Δ -ISW	Δ^N -ISW
1 bin	3.7	3.8
$\Delta z = 0.1$ bins	6.0 (5.3)	6.1 (6.0)

ing high redshift observation. However, this double-counting of information at low redshift is then compensated by includ-

ing the number counts cross-correlation between different redshifts, as previously suggested in LoVerde et al. (2007).

Finally, we plot the cumulative SNR as a function of z_{max} in figure 4. We see that changes in the SNR due to GR terms (mainly lensing) affect the redshift range $z > 1$, where the SNR is still increasing for the galaxy surveys (especially the HI galaxy survey). This means that a cut at $z_{\text{max}} = 2$, where the SNR saturates, does not solve the issue: we have to include in the estimation of the theoretical SNR, the cross-correlation between different redshift bins and include the GR correction to the cross-correlation between number counts/ intensity and ISW signal.

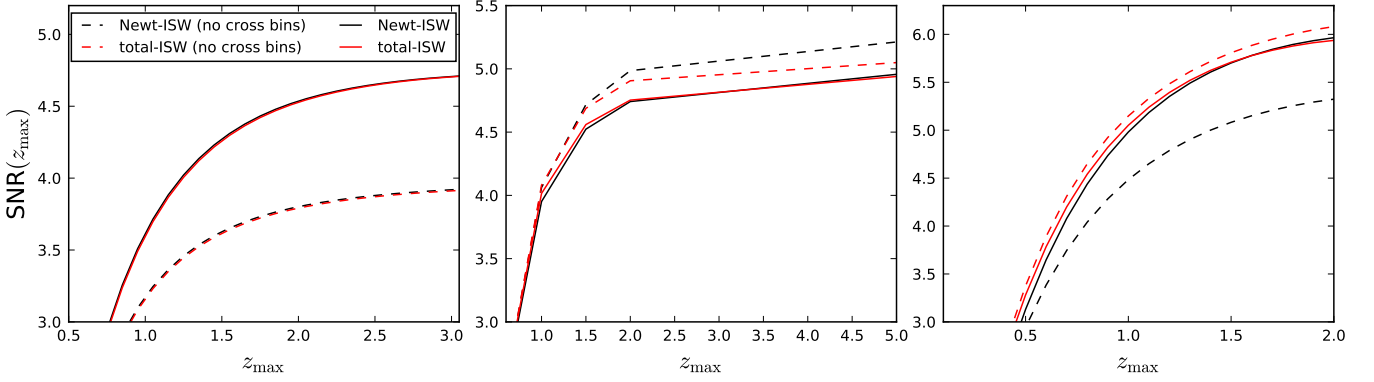


Figure 4. Cumulative SNR up to z_{max} for SKA1 IM (left panel), SKA continuum ($S_{\text{cut}} = 22 \mu\text{Jy}$) (central panel), and SKA2 HI galaxy survey (right panel). Different lines corresponds to the cross-correlation Δ^{N} -ISW (red) and Δ -ISW (black), with and without (dashed) cross-bin correlations.

6 RECONSTRUCTING THE ISW SIGNAL

We use the optimal minimum-variance $\hat{a}_{\ell m}^{\text{ISW}}$ estimator derived in Barreiro et al. (2009); Manzotti & Dodelson (2014) to reconstruct the ISW signal from CMB and LSS maps (see also applications of the same estimators in Muir & Huterer 2016; Weaverdyck et al. 2018):

$$\hat{a}_{\ell m}^{\text{ISW}} = \sum_i R_{\ell}^i a_{\ell m}^i, \quad (30)$$

where $i \in [1, n]$ and the reconstruction filter derived from the covariance matrix is:

$$R_{\ell}^i = -N_{\ell} (D_{\ell}^{-1})_{1,i}. \quad (31)$$

The covariance matrix is:

$$D_{\ell} = \begin{pmatrix} C_{\ell}^{\text{ISW}} & C_{\ell}^{\text{ISW}\Delta_1} & \dots & \dots & C_{\ell}^{\text{ISW}} \\ C_{\ell}^{\Delta_1 \text{ISW}} & \bar{C}_{\ell}^{\Delta_1} & \dots & \dots & C_{\ell}^{\Delta_1 \text{ISW}} \\ \vdots & \vdots & \ddots & \vdots & \vdots \\ C_{\ell}^{\Delta_n \text{ISW}} & \dots & \dots & \bar{C}_{\ell}^{\Delta_n} & C_{\ell}^{\Delta_n \text{ISW}} \\ C_{\ell}^{\text{ISW}} & C_{\ell}^{\text{ISW}\Delta_1} & \dots & \dots & C_{\ell}^{TT} \end{pmatrix} \quad (32)$$

Here the estimated variance of the reconstruction is:

$$N_{\ell} = [(D_{\ell}^{-1})_{1,1}]^{-1}. \quad (33)$$

We reconstruct the ISW using the CMB temperature and n LSS maps.

An example of the reconstructed ISW map is shown in figure 5. The reconstruction using simulated data of a SKA1-MID Band 1 radio continuum survey with $S_{\text{cut}} = 22 \mu\text{Jy}$ with 5 z-bins (corresponding to a SNR ~ 5.0) (central panel), shares a number of the visual features in common with the input ISW map (top panel). For comparison, we show in the bottom panel the ISW reconstruction obtained with the CMB temperature map alone, where only a very large scale feature is captured.

6.1 Reconstruction validation

To quantify the accuracy of a given reconstruction, we use the correlation coefficient between the true ISW map T^{ISW} and the reconstructed ISW map \hat{T}^{ISW} :

$$\rho = \frac{\langle T^{\text{ISW}} \hat{T}^{\text{ISW}} \rangle_{\text{pix}}}{\sigma_{\text{ISW}} \sigma_{\text{rec}}}, \quad (34)$$

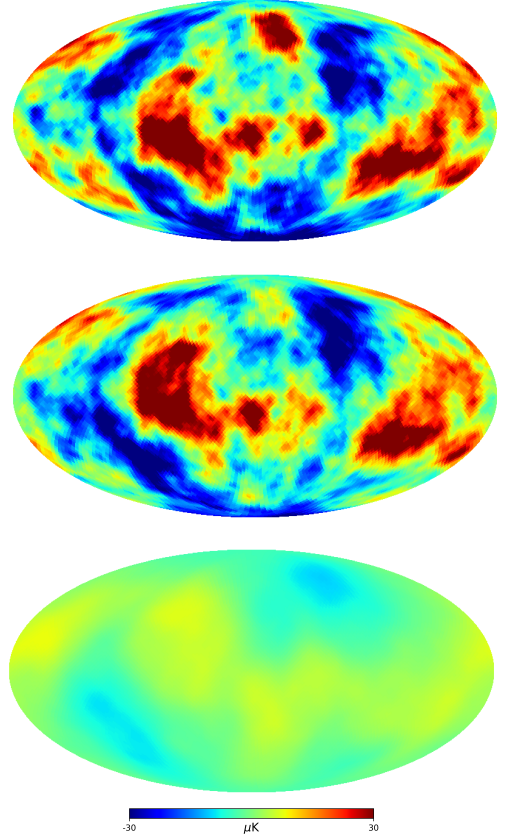


Figure 5. Example of the reconstruction procedure applied to simulations data as described in (30). The top panel shows the input ISW map, the central panel shows the recovered ISW estimate using CMB temperature in combination with SKA1 continuum survey ($S_{\text{cut}} = 22 \mu\text{Jy}$), and the bottom panel shows the recovered ISW estimate using CMB temperature alone. All the maps have a resolution $N_{\text{SIDE}} = 32$.

where σ_{ISW} (σ_{rec}) is the variance of the true (reconstructed) ISW map. We consider also a second statistical estimator, because the estimator (34) is insensitive to changes in the overall amplitude of the reconstructed ISW map. The recon-

structed map residual is defined as:

$$s = \frac{\langle (T^{\text{ISW}} - \hat{T}^{\text{ISW}}) \rangle_{\text{pix}}^{1/2}}{\sigma_{\text{ISW}}}. \quad (35)$$

We calculate ρ and s , averaged over 10,000 simulations, using the following general pipeline:

- Fiducial cosmological model is flat, with best-fit parameters: $\omega_b \equiv \Omega_b h^2 = 0.02218$, $\omega_c \equiv \Omega_c h^2 = 0.1205$, $h_0 = 0.6693$, $\tau = 0.0596$, $n_s = 0.9619$, and $\log(10^{10} A_s) = 3.056$, from the 2015 analysis of *Planck* data (Aghanim et al. 2016). LSS survey specifications are given in section 4.

- Compute the observed auto- and cross-correlation angular power spectra (10), including the GR corrections with a modified version of CAMB_sources² (Challinor & Lewis 2011).

- Generate correlated Gaussian realisations of the CMB and LSS maps using HEALPix³ (Gorski et al. 2005):

$$a_{\ell m}^i = \sum_{j=1}^i \xi_j T_{ij}, \quad (36)$$

where ξ is a complex random number with unit variance $\langle \xi \xi^* \rangle = 1$ and zero mean $\langle \xi \rangle = 0$, satisfying $\langle \xi_i \xi_j^* \rangle = \delta_{ij}$. The amplitudes T_{ij} are generated with the following recursive expression (Giannantonio et al. 2008) to guarantee that any two maps will be correlated:

$$T_{ij} = \left(C^{ji} - \sum_{k=1}^{j-1} T_{ik}^2 \right)^{1/2} \quad \text{if } i = j, \quad (37)$$

$$T_{ij} = (T_{jj})^{-1} \left(C^{ji} - \sum_{k=1}^{j-1} T_{ik} T_{jk} \right) \quad \text{if } i > j, \quad (38)$$

where the index i runs over the number of maps (CMB and LSS).

- The noise for the LSS maps, i.e. shot-noise for the galaxy surveys and instrumental noise for IM, is also generated in the form of $a_{\ell m}^N$ as a Gaussian uncorrelated map with respect to the other fields.

- Construct the covariance (32) with a set of auto- and cross-correlation angular power spectra C_{ℓ}^{XY} . As we did for the SNR estimation, we test both the impact of including the GR corrections (always included in the input maps/ simulations) and neglecting cross-bin correlations in the covariance (32).

- Compare the reconstructed ISW signal to the true ISW map and evaluate the accuracy of the reconstruction by using (34) and (35).

Table 4 shows the quality of the ISW reconstruction for different datasets, where values $\langle \rho \rangle \rightarrow 1$ and $\langle s \rangle \rightarrow 0$ indicate more accurate reconstruction.

We consider full-sky simulations without taking into account of the mask for each single map. Bonavera et al. (2016) show that the reconstruction quality is degraded by incomplete sky coverage input datasets, even when considering spectra corrected using MASTER (Hivon et al. 2002) in order to include the mode coupling in the presence of a mask.

The values of $\langle \rho \rangle$, averaged over 10,000 simulations, follow our finding for the SNR. We find always a higher value of $\langle \rho \rangle$ when tomography is performed, even in those cases, like MeerKLASS and SKA1 continuum surveys, where there is a tiny improvement in terms of SNR. Neglecting the GR terms in the filter for the reconstruction, by using a wrong covariance matrix (32), the recovered map is not properly scaled by the filter and the quality of the reconstruction is worse. However including the cross-correlation between redshift bins compensates for this degradation and we find the same values for $\langle \rho \rangle$, even when GR terms are not included in the theoretical angular power spectra used for the covariance. Moreover the inclusion of the cross-correlation leads to a better reconstruction quality, around $\sim 10 - 20\%$.

Similar findings follow for the average reconstructed map residuals $\langle s \rangle$. The cross-correlation between the number counts and the ISW component of the CMB is affected both in the shape and amplitude at large angular scales, by the lensing convergence contribution to the number counts (see figures 2 and 3). However, this effect becomes important at high redshift $z > 1.5$, which lowers the contribution to the total ISW detection – and for this reason we do not see a significant shift in $\langle s \rangle$ when the wrong covariance matrix is used.

7 CONCLUSION

In this work, we studied the feasibility of detecting the late-time ISW imprinted on the CMB temperature anisotropies by cross-correlating CMB maps with future radio maps from the SKA. Then we investigated the reconstruction of the ISW signal combining CMB with SKA surveys. We considered two of the main three cosmological probes provided by SKA in Phase 1 (Bacon et al. 2018), namely the neutral hydrogen (HI) intensity mapping survey and the radio continuum galaxy survey, together with their two precursor surveys, MeerKLASS (Santos et al. 2017) and EMU (Norris et al. 2011). We also considered the more futuristic SKA2 for radio continuum and the HI galaxy survey (the ‘billion galaxy’ spectroscopic survey).

We began by quantifying the theoretical signal-to-noise ratio (SNR) for ISW detection through angular cross-power spectra of CMB temperature and number counts/ intensity. One of the key factors to maximize the synergy between CMB and LSS maps is to have the largest overlapping sky area, also because $\text{SNR} \propto \sqrt{f_{\text{sky}}}$. Future radio surveys promise to deliver near full-sky maps of the dark matter distribution using HI with sky area $\sim 20,000 - 30,000 \text{ deg}^2$. On the other hand, future optical/ infrared surveys such as DESI (Levi et al. 2013; Aghamousa et al. 2016a,b), Euclid (Laureijs et al. 2011; Amendola et al. 2016) and LSST (Abell et al. 2009; Alonso et al. 2018) have sky area $\sim 15,000 \text{ deg}^2$.

For the IM surveys, we find $1 < \text{SNR} < 2$ (~ 2.2 combining the two Bands) for MeerKLASS and $\text{SNR} \sim 3.7 - 4.7$ for SKA1 in Band 1: see table 1. For the radio continuum galaxy surveys, we find for EMU a $\text{SNR} \sim 5$, a $\text{SNR} \sim 4.0 - 5.0$ for SKA1 in Band 1 and $5.6 - 6.2$ for SKA2: see table 2. For the HI galaxy survey from SKA2 we find a $\text{SNR} \sim 3.7 - 6.0$: see table 3.

We tested the effect on the SNR of a tomographic approach, splitting the information of the surveys in different

² https://github.com/cmbant/CAMB/tree/CAMB_sources

³ <https://github.com/healpy/healpy>

Table 4. Mean reconstruction quality coefficients $\langle\rho\rangle$ and $\langle s\rangle$ of ISW map reconstructions for various combinations of input maps. First column gives the case where GR corrections are included in the estimator. Second column shows results using the Newtonian approximation. Numbers in brackets indicate that no correlations between redshift bins are included.

	$\langle\rho\rangle$		$\langle s\rangle$	
	$R_\ell(\Delta_\ell^{\text{GR}})$	$R_\ell(\Delta_\ell^{\text{N}})$	$R_\ell(\Delta_\ell^{\text{GR}})$	$R_\ell(\Delta_\ell^{\text{N}})$
MeerKLASS L-Band (1 bin)	0.38	0.38	0.93	0.93
MeerKLASS L-Band (5 bin)	0.54 (0.43)	0.54 (0.43)	0.84 (0.91)	0.84 (0.90)
MeerKLASS UHF-Band (1 bin)	0.56	0.56	0.83	0.83
MeerKLASS UHF-Band (11 bin)	0.65 (0.57)	0.65 (0.41)	0.76 (0.87)	0.77 (0.91)
SKA1 - IM (1 bin)	0.55	0.55	0.85	0.85
SKA1 - IM (27 bin)	0.75 (0.66)	0.75 (0.43)	0.63 (0.85)	0.65 (0.90)
EMU (1 bin)	0.63	0.62	0.78	0.78
SKA1 - continuum 22 μJy (1 bin)	0.67	0.67	0.75	0.75
SKA1 - continuum 22 μJy (5 bin)	0.87 (0.78)	0.87 (0.76)	0.53 (0.65)	0.49 (0.65)
SKA1 - continuum 10 μJy (1 bin)	0.93	0.93	0.39	0.37
SKA1 - continuum 10 μJy (5 bin)	0.93 (0.85)	0.93 (0.82)	0.41 (0.55)	0.36 (0.57)
SKA2 - continuum 1 μJy (1 bin)	0.82	0.82	0.58	0.60
SKA2 - continuum 1 μJy (5 bin)	0.90 (0.77)	0.88 (0.84)	0.43 (0.64)	0.54 (0.61)
SKA2 - HI gal (1 bin)	0.60	0.60	0.44	0.49
SKA2 - HI gal (19 bin)	0.90 (0.67)	0.88 (0.53)	0.44 (0.75)	0.49 (0.85)

redshift bins. The results show that tomography does improve the SNR, but mildly and requiring only a small number of broad redshift bins.

Then, we considered the more realistic approach reconstructing the ISW signal using a likelihood based minimum-variance estimator from CMB and LSS maps. We considered the ISW reconstruction from single radio surveys but splitting the surveys in different redshift bins, according to their baseline specifications and consistently with our SNR analysis.

We quantified the accuracy of the reconstruction with two estimators, namely the correlation coefficient between the input and the reconstructed ISW map ρ , and the reconstructed map residual s . We calculated ρ and s , averaging over 10,000 simulations, for all the radio surveys considered, with and without tomography. Our results for $\langle\rho\rangle$ and $\langle s\rangle$ are consistent with our finding for the SNR. Moreover, we find that tomography always leads to a higher quality of the ISW reconstruction for these two estimators, even for those cases where there is not any change in term of SNR, such as for MeerKLASS and SKA1 continuum surveys.

We also studied the impact of observational effects on the radio surveys from lensing magnification, Doppler and other relativistic corrections, in altering the cross-correlation signal from CMB temperature and radio surveys. We found that these effects do alter the angular cross-power spectra of CMB temperature and number counts/ intensity, as seen in figures 1–3; they could change the expected SNR and degrade the ISW reconstruction when they are not modelled in the theoretical covariance used in (14) for the SNR and

used in (30) for the reconstruction (Barreiro et al. 2009; Manzotti & Dodelson 2014).

By including the cross-bin correlations we found a perfect cancellation of the shift in the SNR due to the correlation between high- and low-redshift induced lensing contribution (which dominates the GR effects); see also LoVerde et al. (2007). This impact is also mostly cancelled on $\langle\rho\rangle$ and $\langle s\rangle$. A residual difference is present in $\langle s\rangle$, which is affected by the change of both the shape and the amplitude of the spectrum between the true and reconstructed ISW signal.

There are a number of ways that one could improve the robustness and accuracy of our forecasts.

In this paper, we considered the cross-correlation between the CMB and single radio surveys. Since the estimator (30) is able to combine any numbers of maps as input, it is possible to test the combined effect of all the radio surveys that will be provided from SKA for the ISW detection and reconstruction. However, this multi-tracer application to the ISW has been shown in Ballardini et al. (2019) to be effective for surveys which cover different redshifts, or for tracers with a very different redshift distribution.

The inclusion of maps of the lensing potential has been shown (Cooray 2002; Ferraro et al. 2015; Manzotti & Dodelson 2014; Ade et al. 2016; Bonavera et al. 2016) to have the potential to improve the ISW reconstruction. This will be possible in light of future CMB experiments beyond *Planck*, able to provide better lensing maps in particular at the largest scales, i.e. $\ell < 10$, where the correlation between ISW and lensing is largest (Manzotti & Dodelson 2014).

We conclude that SKA in Phase 1 promises a $\sim 5\sigma$ de-

tection of the ISW signal with 21cm intensity mapping and radio continuum surveys, with a similar forecast for the precursor EMU survey, while a larger significance at $\sim 6\sigma$ will be possible with SKA2 using the 21cm galaxy redshift and radio continuum surveys. Moreover, we find that lensing and other relativistic observation effects on the number counts/intensity angular power spectra have a small impact on the ISW detection and reconstruction. However, their impact on cosmological parameter estimation can be significant (Camera et al. 2015; Cardona et al. 2016; Lorenz et al. 2018).

Acknowledgments

MB thanks R. B. Barreiro, C. A. P. Bengaly, L. Bonavera, S. Camera, F. Finelli, A. Manzotti, D. Molinari, M. Spinelli and C. Umiltà for fruitful discussions. MB and RM were supported by the South African Radio Astronomy Observatory, which is a facility of the National Research Foundation, an agency of the Department of Science and Technology. MB is also supported by a Claude Leon Foundation fellowship and by ASI n.I/023/12/0 "Attività relative alla fase B2/C per la missione Euclid". RM is also supported by the UK Science & Technology Facilities Council (Grant ST/N000668/1).

REFERENCES

- Abell P. A., et al., 2009. ([arXiv:0912.0201](#))
- Ade P. A. R., et al., 2014, *Astron. Astrophys.*, 571, A19
- Ade P. A. R., et al., 2016, *Astron. Astrophys.*, 594, A21
- Afshordi N., 2004, *Phys. Rev.*, D70, 083536
- Afshordi N., Loh Y.-S., Strauss M. A., 2004, *Phys. Rev.*, D69, 083524
- Aghamousa A., et al., 2016b. ([arXiv:1611.00036](#))
- Aghamousa A., et al., 2016a. ([arXiv:1611.00037](#))
- Aghanim N., et al., 2016, *Astron. Astrophys.*, 596, A107
- Alonso D., Bull P., Ferreira P. G., Maartens R., Santos M., 2015, *Astrophys. J.*, 814, 145
- Alonso D., et al., 2018. ([arXiv:1809.01669](#))
- Amendola L., et al., 2016. ([arXiv:1606.00180](#))
- Bacon D. J., et al., 2018. ([arXiv:1811.02743](#))
- Baldauf T., Seljak U., Desjacques V., McDonald P., 2012, *Phys. Rev.*, D86, 083540
- Ballardini M., Finelli F., Maartens R., Moscardini L., 2018, *JCAP*, 1804, 044
- Ballardini M., Paoletti D., Finelli F., Moscardini L., Sartoris B., Valenziano L., 2019, *Mon. Not. Roy. Astron. Soc.*, 482
- Barreiro R. B., Vielva P., Hernandez-Monteagudo C., Martinez-Gonzalez E., 2009, *Radio Sci.*, 44, 5004
- Barreiro R. B., Vielva P., Marcos-Caballero A., Martinez-Gonzalez E., 2013, *Mon. Not. Roy. Astron. Soc.*, 430, 259
- Battye R. A., Davies R. D., Weller J., 2004, *Mon. Not. Roy. Astron. Soc.*, 355, 1339
- Bernal J. L., Raccanelli A., Kovetz E. D., Parkinson D., Norris R. P., Danforth G., Schmitt C., 2018. ([arXiv:1810.06672](#))
- Bianchini F., Renzi A., Marinucci D., 2016, *JCAP*, 1611, 050
- Bonavera L., Barreiro R. B., Marcos-Caballero A., Vielva P., 2016, *Mon. Not. Roy. Astron. Soc.*, 459, 657
- Boughn S., Crittenden R., 2004, *Nature*, 427, 45
- Bruni M., Crittenden R., Koyama K., Maartens R., Pitrou C., Wands D., 2012, *Phys. Rev.*, D85, 041301
- Bull P., Ferreira P. G., Patel P., Santos M. G., 2015, *Astrophys. J.*, 803, 21
- Camera S., Santos M. G., Maartens R., 2015, *Mon. Not. Roy. Astron. Soc.*, 448, 1035
- Cardona W., Durrer R., Kunz M., Montanari F., 2016, *Phys. Rev.*, D94, 043007
- Challinor A., Lewis A., 2011, *Phys. Rev.*, D84, 043516
- Chang T.-C., Pen U.-L., Peterson J. B., McDonald P., 2008, *Phys. Rev. Lett.*, 100, 091303
- Cooray A., 2002, *Phys. Rev.*, D65, 103510
- Crittenden R. G., Turok N., 1996, *Phys. Rev. Lett.*, 76, 575
- Ferraro S., Sherwin B. D., Spergel D. N., 2015, *Phys. Rev.*, D91, 083533
- Fonseca J., Camera S., Santos M., Maartens R., 2015, *Astrophys. J.*, 812, L22
- Fonseca J., Maartens R., Santos M. G., 2018, *Mon. Not. Roy. Astron. Soc.*, 479, 3490
- Fosalba P., Gaztanaga E., 2004, *Mon. Not. Roy. Astron. Soc.*, 350, L37
- Frommert M., Ensslin T. A., 2008. ([arXiv:0811.4433](#))
- Giannantonio T., Scranton R., Crittenden R. G., Nichol R. C., Boughn S. P., Myers A. D., Richards G. T., 2008, *Phys. Rev.*, D77, 123520
- Giannantonio T., Crittenden R., Nichol R., Ross A. J., 2012, *Mon. Not. Roy. Astron. Soc.*, 426, 2581
- Gorski K. M., Hivon E., Banday A. J., Wandelt B. D., Hansen F. K., Reinecke M., Bartelman M., 2005, *Astrophys. J.*, 622, 759
- Granett B. R., Neyrinck M. C., Szapudi I., 2008, *Astrophys. J.*, 683, L99
- Hall A., Bonvin C., Challinor A., 2013, *Phys. Rev.*, D87, 064026
- Hernandez-Monteagudo C., 2010, *Astron. Astrophys.*, 520, A101
- Hivon E., Gorski K. M., Netterfield C. B., Crill B. P., Prunet S., Hansen F., 2002, *Astrophys. J.*, 567, 2
- Ho S., Hirata C., Padmanabhan N., Seljak U., Bahcall N., 2008, *Phys. Rev.*, D78, 043519
- Ilic S., Douspis M., Langer M., Penin A., Lagache G., 2011, *Mon. Not. Roy. Astron. Soc.*, 416, 2688
- Jeong D., Schmidt F., Hirata C. M., 2012, *Phys. Rev.*, D85, 023504
- Karagiannis D., Lazanu A., Liguori M., Raccanelli A., Bartolo N., Verde L., 2018, *Mon. Not. Roy. Astron. Soc.*, 478, 1341
- Knox L., 1995, *Phys. Rev.*, D52, 4307
- Kofman L., Starobinsky A. A., 1985, *Sov. Astron. Lett.*, 11, 271
- Kovetz E. D., et al., 2017. ([arXiv:1709.09066](#))
- Laureijs R., et al., 2011. ([arXiv:1110.3193](#))
- Levi M., et al., 2013. ([arXiv:1308.0847](#))
- LoVerde M., Hui L., Gaztanaga E., 2007, *Phys. Rev.*, D75, 043519
- Lorenz C. S., Alonso D., Ferreira P. G., 2018, *Phys. Rev.*, D97, 023537
- Maartens R., Zhao G.-B., Bacon D., Koyama K., Raccanelli A., 2013, *JCAP*, 1302, 044
- Maartens R., Abdalla F. B., Jarvis M., Santos M. G., 2015, *PoS, AASKA14*, 016
- Manzotti A., Dodelson S., 2014, *Phys. Rev.*, D90, 123009
- McEwen J. D., Vielva P., Hobson M. P., Martinez-Gonzalez E., Lasenby A. N., 2007, *Mon. Not. Roy. Astron. Soc.*, 376, 1211
- Muir J., Huterer D., 2016, *Phys. Rev.*, D94, 043503
- Nolta M. R., et al., 2004, *Astrophys. J.*, 608, 10
- Norris R. P., et al., 2011, *Publ. Astron. Soc. Austral.*, 28, 215
- Papai P., Szapudi I., Granett B. R., 2011, *Astrophys. J.*, 732, 27
- Pourtsidou A., Bacon D., Crittenden R., 2017, *Mon. Not. Roy. Astron. Soc.*, 470, 4251
- Raccanelli A., et al., 2012, *Mon. Not. Roy. Astron. Soc.*, 424, 801
- Raccanelli A., et al., 2015, *JCAP*, 1501, 042
- Raccanelli A., Montanari F., Bertacca D., Dorl O., Durrer R., 2016, *JCAP*, 1605, 009
- Renk J., Zumalacarregui M., Montanari F., 2016, *JCAP*, 1607, 040
- Sachs R. K., Wolfe A. M., 1967, *Astrophys. J.*, 147, 73
- Santos M., et al., 2015, *PoS, AASKA14*, 019
- Santos M. G., et al., 2017, in *Proceedings, MeerKAT Science:*

- On the Pathway to the SKA (MeerKAT2016): Stellenbosch, South Africa, May 25-27, 2016. ([arXiv:1709.06099](#))
- Schiavon F., Finelli F., Gruppuso A., Marcos-Caballero A., Vielva P., Crittenden R. G., Barreiro R. B., Martinez-Gonzalez E., 2012, *Mon. Not. Roy. Astron. Soc.*, 427, 3044
- Shajib A. J., Wright E. L., 2016, *Astrophys. J.*, 827, 116
- Stölzner B., Cuoco A., Lesgourgues J., Bilicki M., 2018, *Phys. Rev.*, D97, 063506
- Taburet N., Hernandez-Monteagudo C., Aghanim N., Douspis M., Sunyaev R. A., 2011, *Mon. Not. Roy. Astron. Soc.*, 418, 2207
- Vielva P., Martinez-Gonzalez E., Tucci M., 2006, *Mon. Not. Roy. Astron. Soc.*, 365, 891
- Weaverdyck N., Muir J., Huterer D., 2018, *Phys. Rev.*, D97, 043515
- Wilman R. J., et al., 2008, *Mon. Not. Roy. Astron. Soc.*, 388, 1335
- Wyithe S., Loeb A., 2008, *Mon. Not. Roy. Astron. Soc.*, 383, 606

This paper has been typeset from a \LaTeX file prepared by the author.